NUMERICAL INVESTIGATION OF HEAT TRANSFER PERFORMANCE IN PARALLEL AND SYMMETRIC WAVY MICROCHANNEL HEAT SINKS

DongQing DAI[1], JinRong ZHU [*], Hui LI [2], ShiJun MA[3], Hui LV[4] and Qinghua LV[5]

School of Science, Hubei University of Technology, Wuhan, China

[*]Corresponding author; E-mail: jinrzhu@sina.com

Microchannel heat sinks have advantages such as a high surface area-to-volume ratio, a large heat transfer coefficient, and lightweight design, making them crucial for microelectronics and aerospace applications. Numerical simulation was conducted to analyze the fluid flow and heat transfer characteristics in the newly designed heat sink at Reynolds number ranging from 147 to 736. The symmetric wavy microchannel heat sinks were compared with the parallel wavy microchannel heat sinks based on friction coefficient, Nusselt number, and comprehensive performance factor. The results indicate that periodic variation in the cross-sectional area of the symmetric wavy microchannels generates vortices at the valleys, enhancing fluid mixing. In contrast, the fluid in the parallel wavy microchannels exhibits a wave-type flow pattern, where the wavy structure disrupts the flow boundary layer. The fluid flows along the streamlined boundary with less flow friction. This enables heat transfer enhancement under lower pressure drop conditions. The geometrical parameters for optimal heat transfer performance are obtained by adjusting the amplitude ratio (α). The comprehensive performance factor for the parallel wavy microchannels, with a Reynolds number of 736 and a value of α = 4, is 1.64.

Key words: *microchannel heat sink, heat transfer enhancement, wavy microchannel, numerical simulation*

1. Introduction

As electronic devices improve in performance and become more compact, thermal management has taken over as a major issue. MCHS provides a solution for chip heat dissipation with high efficiency, compactness, and coolant savings. Tuckerman and Pease began working on MCHS cooling technology in 1981 [1]. In a conventional straight rectangular microchannel, the fluid flows almost steadily. During the flow process, the thermal boundary layer becomes progressively thicker. The convective heat transfer between the fluid and the microchannel's inner surface will be weakened [2]-[4].

Cavities are an effective way to enhance heat transfer by interrupting the flow boundary layer. Kumar *et al*. [5] studied the effect of cavity depth on fluid flow and heat transfer behavior of rectangular MCHSs. Cavities in the sidewalls of the channel result in a 119% increase in the Nusselt number. Zhu *et al*. [6] investigated the influence of geometrical parameters of trapezoidal cavities in the side walls of microchannels on the fluid flow and heat transfer characteristics. It was found that the denser the distribution of cavities, the lower the bottom wall temperature. The effect of trapezoidal cavity depth on the overall performance is greater than the relative cavity spacing. Yan Hao SOO *et al*. [7] investigated the

heat transfer performance of microchannels with staggered water droplet cavities. It was found that the reason for the enhanced heat transfer was the formation of vortices in water droplet cavities and the increase in heat transfer area between the fluid and the solid.

Ribs can alter the velocity distribution of fluid within the microchannels, enhancing the disturbance to the fluid[8]-[10]. Based on this concept, the effects of slant rectangular ribs on straight and wavy MCHSs were investigated by Wang *et al*. [11]. The findings indicate that the fluid thermal boundary was interrupted, and the heat transfer area of the heat sink was increased. Khoshvaght-Aliabadi *et al*. [12] consider the influence of pin-fin on heat sinks in straight and wavy microchannels. The results showed that pin-fin can hinder the development of the flow boundary layer. Venkiteswaran *et al*. [13] investigated the fluid flow characteristics in parallel and staggered rectangular rib microchannel heat sinks. They found that the staggered rib arrangement induces periodic changes in the flow direction, leading to local recirculation and enhanced mixing of the hot fluid near the channel walls with the colder fluid at the center.

Due to the large pressure drop caused by the addition of ribs to the microchannels, combinations of cavities and ribs can be added to microchannels to minimize pressure drop[14][15]. Datta *et al*. [16] studied heat transfer performance of MCHSs with trapezoidal cavities and ribs combinations. The results showed that the combination of trapezoidal cavities and diamond ribs were optimal structures for heat dissipation. This structure has the potential to significantly enhance the comprehensive performance coefficient of MCHS. Zhu *et al*. [17] studied the heat transfer performance of MCHSs with water droplet cavities combined with different ribs. Microchannels with rectangular ribs exhibit the highest pressure drop and Nusselt number. The microchannels combining teardrop cavities and elliptical ribs achieve the highest comprehensive performance factor of 1.51. Jiang *et al*. [18] designed a microchannel heat sink with trapezoidal cavities and elliptical ribs. The optimized microchannel heat sinks exhibit a 14.86% reduction in pressure drop compared to the original design. This lower pressure drop decreases both pump power consumption and the risk of leakage.

MCHS with cavities and ribs are used to achieve heat transfer enhancement by increasing the heat transfer area and disturbing the boundary layer. The goal of an increase in heat transfer area and disturbance of the boundary layer can now also be achieved by changing the shape of the channel. Wavy microchannels have the potential to enhance heat transfer performance by inducing vortex formation in fluids as they flow through the peaks and valleys of the channel. Sui *et al*. [19][21] conducted studies on wavy microchannels with rectangular cross-sections and observed that an increase in the Reynolds number significantly enhances fluid mixing. Xie *et al*. [22] optimized the geometry of the asymmetric wavy MCHS to reduce the global thermal resistance by changing the wavelength ratio and amplitude ratio. The wavy microchannels had the minimum thermal resistance at $Re = 200$, with a wavelength ratio of 0.8, and an amplitude ratio of 1. Zhou *et al*. [23] investigated MCHS with a sinusoidal wave structure and found that the highest heat transfer performance was achieved at an amplitude of 0.04 mm and a wavelength of 0.1 mm by adjusting the amplitude and wavelength of the wavy microchannels. Ali *et al*. [24] designed a convergent-divergent MCHS for high concentrator photovoltaic modules. The findings indicated that the new MCHS exhibited a higher heat transfer rate and could reduce the average temperature of the cell by 11.4% compared to the straight rectangular MCHS. Wang *et al*. [25] experimentally examined the hydrothermal characteristics of semi-sinusoidal corrugated copper microchannels. They discovered that an increase in wave amplitude and a decrease in wavelength led to an increase in the heat transfer area of the microchannels. However, the increase in wave number also leads to an increase

of flow friction. Fang *et al*. [26] investigated the effect of an S-shaped channel on flow and heat transfer characteristics. The results show that compared with smooth microchannels, the pressure drop of S-shaped microchannels increases by 234.6% - 774.3%, the average Nusselt number increases by 11.1% - 98.6%, and the total thermal resistance decreases by 10.08% - 50.15%.

Based on the above study, it has been found that wavy microchannels exhibit superior heat transfer performance compared to straight rectangular microchannels with the same hydraulic diameter. Studies also indicate that wavy channels can achieve higher heat transfer efficiency under lower pressure drop conditions. The curved walls of wavy microchannels generate vortices that enhance fluid mixing. Existing research has primarily focused on sinusoidal or fixed-amplitude wavy channels, whereas this study pioneers the investigation of parallel and symmetric wavy microchannels with variable amplitude ratios (α). The newly designed waveform boundaries are generated by superimposing two sinusoidal functions, allowing the adjustment of waveform geometry to optimize vortex formation and boundary layer disruption—a feature not previously explored in the literature. This paper proposes a novel variable-amplitude wavy microchannel heat sink and examines the effects of different geometric parameters in parallel and symmetric configurations on fluid flow and heat transfer performance. Compared to the symmetric design, the parallel configuration reduces flow pressure drop, thereby enabling efficient heat transfer at lower pumping power.

2. Mathematical model of microchannel heat sink

The MCHS consists of 10 aluminum microchannels. Based on geometric symmetry, one microchannel is used as a computational domain. Figure 1 shows schematic diagrams of four types of MCHSs. The main dimensions of the MCHS, including the length L, width W, and height H of the computational domain, are 10 mm, 0.3 mm, and 0.35 mm, respectively. The height of the channel H_c is 0.2 mm, and the width of channel W_c is 0.1 mm. Table 1 lists all the geometric parameters.

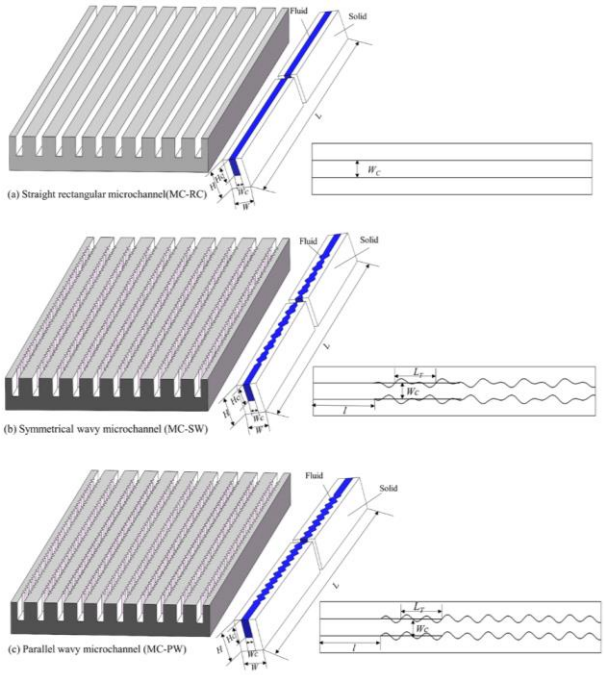

Figure 1. Schematic diagrams of physical models; (a) Straight rectangular microchannel (MC-RC), (b) Symmetric wavy microchannel (MC-SW), (c) Parallel wavy microchannel (MC-PW)

The two wavy boundaries $y = A\,sin(5\pi x) + B\,sin(10\pi x)$ for the parallel configuration microchannel ; $y = A\,sin(5\pi x) + B\,sin(10\pi x)$,and $y = -A\,sin(5\pi x) - B\,sin(10\pi x)$ for the symmetric configuration microchannel. Amplitude ratio $\alpha = B/A$. When B = 0.005 mm, A ranges from 0.005 to 0.06 mm; When B = 0.01 mm, A ranges from 0.005 to 0.02 mm; When B = 0.015 mm, A ranges from 0.005 to 0.01 mm; When B = 0.04 mm, A = 0.01 mm; When B = 0.05 mm, A = 0.005 mm, and amplitude A, B take the value of Table 2.

Table 1. The geometric parameters of MC-PWRR MCHS

Geometric parameters	H [mm]	W [mm]	L [mm]	H_c [mm]	W_c [mm]	l [mm]
Value	0.35	0.3	10	0.2	0.1	0.6

Table 2. Values of the amplitudes *A, B*

B/mm	0.005	0.01	0.015	0.04	0.05
A/mm	0.005-0.06	0.005-0.02	0.005-0.01	0.01	0.005

3. Numerical method

Ansys fluent 15.0 was used as the solver, and the solution was based on the following reasonable assumptions. (1) The fluid is Newtonian and incompressible. (2) The fluid flow and heat transfer are in a steady state. (3) The thermophysical properties of the material remain unchanged. (4) Neglect viscous dissipation and gravity. (5) Neglect radiative heat transfer.

3.1. Governing equations

Based on the previous assumptions, the governing equations are as follows.

Continuity equation:

$$\nabla \cdot (\rho_{\mathrm{f}} \vec{V}) = 0 \tag{1}$$

Where U is the fluid velocity vector and ρ_{f} is the fluid density.

Momentum equations:

$$\nabla \cdot (\rho_{\mathrm{f}} \vec{V} \cdot \nabla \vec{V}) = -\nabla p + \nabla \cdot \mu_{\mathrm{f}} \left[(\nabla \vec{V} + \nabla \vec{V}) - 2/3 \nabla \cdot \vec{V} \right] + \rho_{\mathrm{f}} \vec{g} \tag{2}$$

Where μ_{f} is the fluid dynamic viscosity and P is the fluid pressure.

Energy equation:

$$\nabla \cdot [\rho_{\mathrm{f}} c_{\mathrm{p,f}} (\vec{V} \nabla T)] = \nabla \cdot (k_{\mathrm{f}} \nabla T) \tag{3}$$

Where $C_{\mathrm{p,f}}$ is the specific heat of the fluid, T_{f} is the temperature of the fluid, and λ_{f} is the thermal conductivity of the fluid.

In this paper, the finite volume method was employed to discretize the governing equations with second order upwind scheme. Pressure-velocity coupling was accomplished using the SIMPLIC algorithm. To maintain the convergence of numerical simulations, the residual criterions were set to be 10^{-6} for all variables. Boundary conditions are set as follows. The inlet velocity condition is applied with different uniform values (V_{in} = 1–5 ms^{-1}) and inlet constant temperature (T_{in} = 293 K). The outlet is set to a pressure outlet (p = 1.013 × 10^5 Pa). A constant wall heat flux is applied to the surface of the heated

substrate (q_w = 10^6 Wm^{-2}). Use symmetric boundary conditions on both sidewalls. Other external surfaces are set to be adiabatic walls.

3.2. Grid independence test

Figure 2 shows the grid structure of MC-SW and MC-PW when, Re = 441, α = 2, grid independence test is carried out for MC-PW as an example, and the microchannel is numerically studied using the grid numbers 407772, 1063956, 1273467, 1625980, and 2032541, respectively, and the results of the grid independence validation are shown in Table 3.

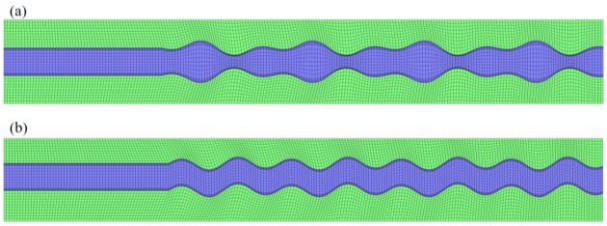

Figure 2. (a) Schematic diagram of MC-PW grid, (b) Schematic diagram of MC-SW grid

Compared with the numerical simulation results obtained when the grid number is 2032541, the relative errors of the overall pressure drop of the microchannel and the average temperature of the substrate when the grid number is 1625980 are 0.361% and 0.021%, respectively. Selecting the number of grids in the computational domain of 1625980 can satisfy the computational accuracy. The relative error (e) can be defined as:

$$e\% = \left|\frac{J_2 - J_1}{J_1}\right| \times 100 \tag{4}$$

J_1 is the physical quantity at grid number 2032541 and J_2 is the physical quantity at other grid numbers.

Table 3. Grid independence verification results of microchannels

Grid number	Pressure drop [Pa]	Relative error [$e\%$]	Temperature of the substrate [K]	Relative error [$e\%$]
407772	268952	9.473	307.882	0.285
1063956	242546	1.275	308.155	0.053
1273467	248522	1.158	307.882	0.036
1625980	246565	0.361	307.927	0.021
2032541	245678	0	307.992	0

3.3. Data acquisition

To calculate the fluid flow and heat transfer characteristics within the microchannel, the corresponding analytical expressions are given.

The Reynolds number (Re) can be expressed as follows:

$$\mathrm{Re} = \frac{\rho u D_h}{\mu} \tag{5}$$

The hydraulic diameter (D_h) can be expressed as follows:

$$D_{\mathrm{h}} = \frac{2H_{\mathrm{c}}W_{\mathrm{c}}}{H_{\mathrm{c}}+W_{\mathrm{c}}} \tag{6}$$

The friction factor (f) can be expressed as follows:

$$f = \frac{2\Delta p D_h}{L\rho u_m^2} \tag{7}$$

The average heat transfer coefficient (h_{m}) and Nusselt number (Nu) are calculated as:

$$h_{\mathrm{m}} = \frac{q_{\mathrm{w}}A_{\mathrm{q}}}{A_{\mathrm{con}}(T_{\mathrm{w}}-T_{\mathrm{f}})} \tag{8}$$

$$\mathrm{Nu} = \frac{h_{\mathrm{m}}D_{\mathrm{h}}}{k_{\mathrm{f}}} \tag{9}$$

3.4. Data acquisition Validation of numerical simulation

To verify the accuracy of available numerical simulations, the pressure drop (Δp) and friction factor (f) of MC-RC were theoretically verified. Under laminar flow conditions, the pressure drop and friction factor can be calculated by the following equations[27][28].

$$\Delta p = \frac{(f\ \mathrm{Re})\mu u_{\mathrm{m}}L}{2{D_{\mathrm{h}}}^2} + \frac{K\rho u_{\mathrm{m}}^2}{2} \tag{10}$$

$$f\mathrm{Re} = \sqrt{[\frac{0.8}{L/\mathrm{Re}D_{\mathrm{h}}}]^2 + (P_{\mathrm{o}})^2} \tag{11}$$

$$P_{\mathrm{o}} = 24\begin{bmatrix}1 - 1.3553(\alpha_{\mathrm{c}}) + 1.9467(\alpha_{\mathrm{c}})^2 - 1.7012(\alpha_{\mathrm{c}})^3 \\ +0.9564(\alpha_{\mathrm{c}})^4 - 0.2537(\alpha_{\mathrm{c}})^5\end{bmatrix} \tag{12}$$

$$K = 0.6796 + 1.2197(\alpha_{\mathrm{c}}) + 3.3089(\alpha_{\mathrm{c}})^2 - 9.5921(\alpha_{\mathrm{c}})^3 + 8.9089(\alpha_{\mathrm{c}})^4 - 2.9959(\alpha_{\mathrm{c}})^5 \tag{13}$$

$$\alpha_{\mathrm{c}} = W_{\mathrm{c}}/H_{\mathrm{c}} \tag{14}$$

Figure 3 illustrates the comparison between numerical simulation and theoretical results for different Re. The pressure drop (Δp) and friction factor (f) can be obtained from Eqs. (10) and (11). Figure 3(a) compares the simulated pressure drop with the theoretical value. The two curves exhibit a similar trend, and the maximum error between them is less than 8.6%. Figure 3(b) compares the simulated friction factor with the theoretical value, showing that the maximum error between the two is less than 7.71%. Therefore, the numerical methods can effectively predict the flow characteristics of MCHSs.

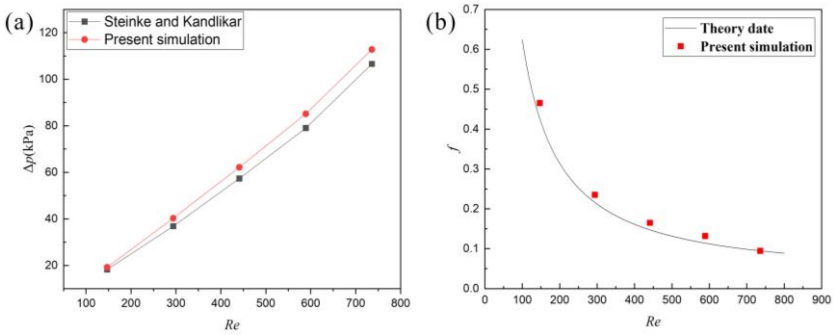

Figure 3. Comparison of numerical simulation results of MC-RC in this paper with results of existing studies; (a) Pressure drop (b) Friction factor

4. Results and discussions

4.1. Effects of amplitude ratio α on velocity distribution and streamlines in microchannels

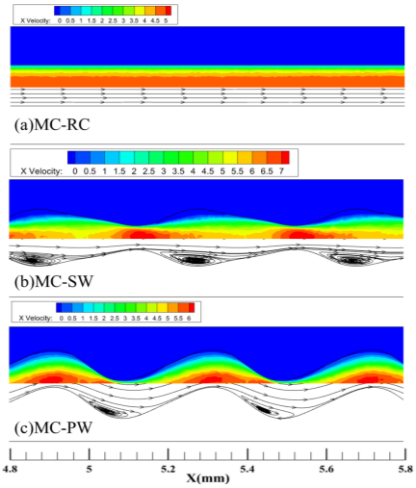

Figure 4. Velocity and streamline distribution in *x*-*z* plane (*y* = 0.25 mm) at Re = 441; (a) MC-RC, (b) MC-SW (*α* = 0.125), (c) MC-PW (*α* = 4)

As shown in Fig. 4, in MC-RC, when the fluid flows along the straight wall, the flow boundary layer is fully developed, which increases the fluid velocity in the center region of the microchannel and decreases the fluid velocity close to the sidewalls. In MC-SW, the microchannel features a notch that expands and then contracts, the velocity along the flow direction shows a periodic increase and decrease, with the maximum velocity at the narrowest section. Due to a change in the direction of fluid flow, flow recirculation occurs at the troughs, generating vortices and forming large recirculation zones. These vortices enhance fluid mixing, thereby improving heat transfer performance. In MC-PW, the fluid flow is influenced by the curved wall surfaces, resulting in a distinct velocity distribution. Near the crest regions, the velocity is higher, driving the fluid towards the troughs, while at the trough regions, the velocity decreases, causing the fluid to shift back towards the crests. This creates an uneven velocity distribution across the entire fluid domain. Significant velocity variations are concentrated near the crests and troughs, whereas the velocity remains relatively stable in the middle flat regions. Multiple vortex regions form due to velocity gradients and uneven pressure distribution. These vortices disrupt flow stability and enhance fluid mixing, thereby improving heat transfer performance.

4.2. Effects of amplitude ratio α on temperature distribution

As shown in Figure 5, the temperature boundary layer in MC-RC thickens progressively along the flow direction, resulting in a larger temperature gradient in the *z*-direction. The temperature within the microchannel increases gradually from the central region toward the sidewalls, with the highest temperature observed near the side walls. In MC-SW, the temperature in the expansion region of the channel is slightly higher than in the contraction region, with the highest temperature occurring near the troughs. Due to fluid viscosity, the change in flow direction reduces water velocity, inducing recirculation and forming stagnation zones near the troughs. These stagnation zones result in localized high-

temperature regions in the expansion sections of the cavities. In MC-PW, the periodically distributed wavy structure causes the fluid to interrupt the boundary layer at each wave crest position, after which it will redevelop, and the periodic interruption and development of the boundary layer can enhance heat transfer performance. Localized high-temperature zones appear at a wall of microchannel between a crest and the trough, due to the return flow of the fluid through the trough. This results in the formation of a stagnation zone, which is not conducive to the removal of heat from the wall by fluid, resulting in an increase in the temperature at this location.

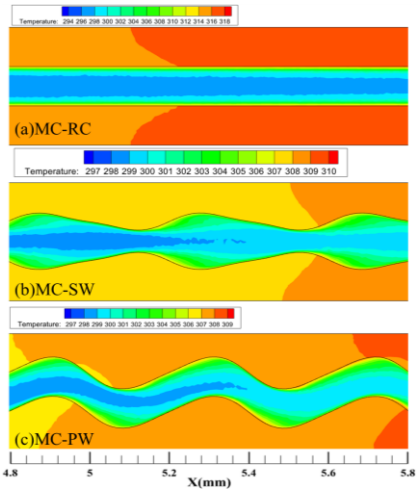

Figure 5. Temperature distribution in *x*-*z* plane (*y* = 0.25 mm) at Re = 441; (a) MC-RC, (b) MC-SW (*α* = 0.125), (c) MC-PW (*α* = 4)

4.3. Effects of amplitude ratio α on pressure distribution

As shown in Figure 6, the pressure in the microchannel decreases approximately linearly along the flow direction due to frictional losses, in MC-RC. In MC-SW, in the expansion section of the cavities, the fluid moves away from the microchannel walls, creating low-pressure regions. In the contraction section of the cavities, the fluid impacts the microchannel walls, creating high-pressure regions. The parallel structured wavy microchannel and rectangular straight microchannel have the same cross-sectional area of the fluid domain. However, the presence of crests and troughs increases frictional losses, leading to a significantly higher overall pressure drop in the wavy microchannel than in the rectangular straight microchannel. In MC-PW, pressure is lower in crest regions and higher in the trough regions, with pressure gradually increasing between the crests and troughs.

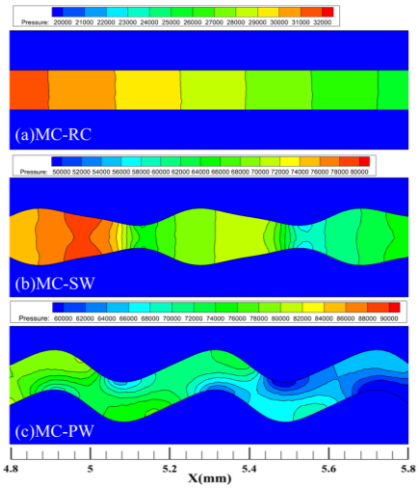

Figure 6. Pressure distribution in *x*-*z* plane (*y* = 0.25 mm) at Re = 441; (a) MC-RC, (b) MC-SW (*α* = 0.125), (c) MC-PW (*α* = 4)

4.4. Effects of α on thermal-hydraulic performance

The comprehensive performance factor is defined by comparing it with the corresponding MC-RC. The comprehensive performance factor *PEC* for microchannel heat transfer is calculated as[29][30]:

$$PEC = \frac{\mathrm{Nu}/\mathrm{Nu}_0}{(f/f_0)^{1/3}} \tag{15}$$

Where: Nu_0 and f_0 are the average Nusselt number and friction factor of MC-RC, Nu and f are the average Nusselt number and friction factor of wavy microchannel.

As shown in Figure 7, the α ranges from 0.5 to 0.2, during which the ratio f/f_0 increases gradually as α decreases. For α below 0.2, the narrowing of the channel in the MC-SW causes f/f_0 to rise sharply, significantly increasing the flow friction factor within the microchannel. For α ranging from 1 to 5, f/f_0 increases gradually as α increases. This behavior is influenced by the continuous change in the cross-sectional area of the microchannel along the flow direction in MC-SW. Additionally, the friction factor

ratio of the symmetric structure is higher than that of the parallel structure. This is due to the flow obstruction caused by stagnation zones, which rapidly increases the friction factor.

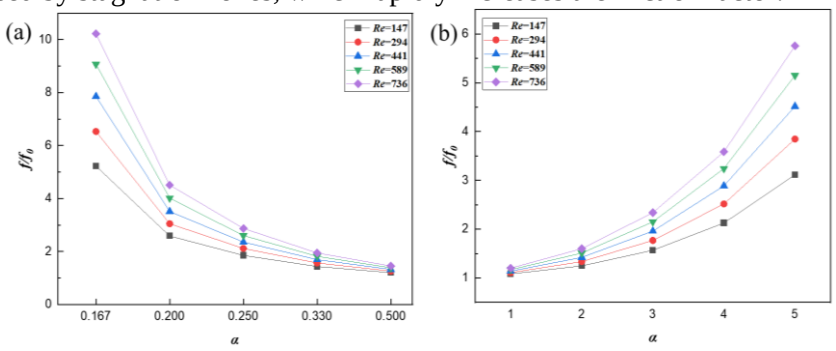

Figure 7. Variation of friction factor ratio f/f_0 of MC-SW with amplitude ratio α at (a) $\alpha < 1$, (b) $\alpha \geq 1$

As shown in Figure 8, for different wavy microchannels, Nu/Nu_0 is greater than 1, indicating that the heat transfer performance of MC-PW is superior to that of MC-RC. In a range of α from 0.167 to 0.5, Nu/Nu_0 decreases with increasing α. In the range of α from 1 to 5, Nu/Nu_0 increases with increasing α. For all cases, the Nusselt number increases with the increase of Reynolds number.

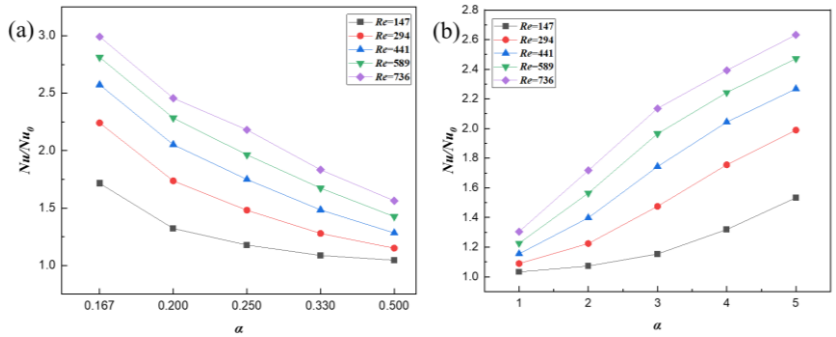

Figure 8. Variation of Nusselt number ratio Nu/Nu_0 of MC-SW with amplitude ratio α at (a) $\alpha < 1$, (b) $\alpha \geq 1$

As shown in Figure 9, *PEC* decreases with α when Re = 736, $0.25 < \alpha < 0.5$. This is because the low velocity significantly increases the friction factor of the microchannel in MC-SW, resulting in a decrease in *PEC*. Re > 147, $1 < \alpha < 3$, *PEC* increases with increase of α. With increase of α, the friction factor increases rapidly, resulting in the slowing down of the increase of *PEC*, Re = 736, $\alpha = 3$, *PEC* takes the maximum value of 1.61. When Re = 736, $\alpha > 3$, the *PEC* of MC-SW decreases with the increase of α. Influenced by the obstruction effect, the pressure drop of the microchannel increases greatly with wavy, which makes comprehensive performance factor of microchannel decrease.

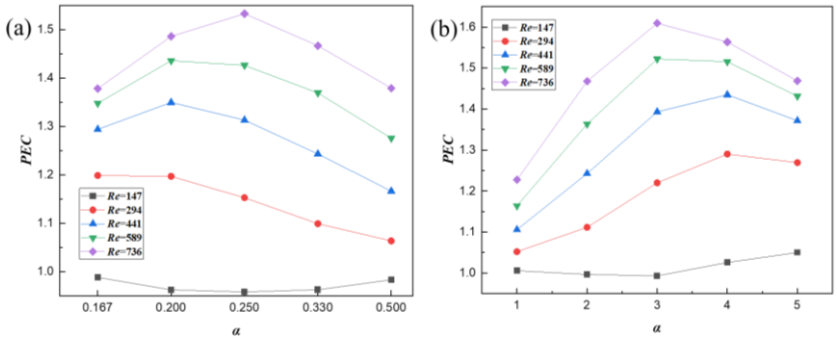

Figure 9. Variation of comprehensive performance factor *PEC* of MC-SW with amplitude ratio α at (a) $\alpha < 1$, (b) $\alpha \geq 1$

As shown in Figure 10, it can be found from the figure that α ranges from 0.17 to 0.5, and f/f_0 increases gradually as α decreases, and $\alpha < 0.17$, and f/f_0 increases rapidly as α decreases. As α decreases, the curvature amplitude of the MC-PW channel increases, causing a rapid increase in flow friction within the fluid channel. In the range of α from 1 to 5, f/f_0 increases with increasing α.

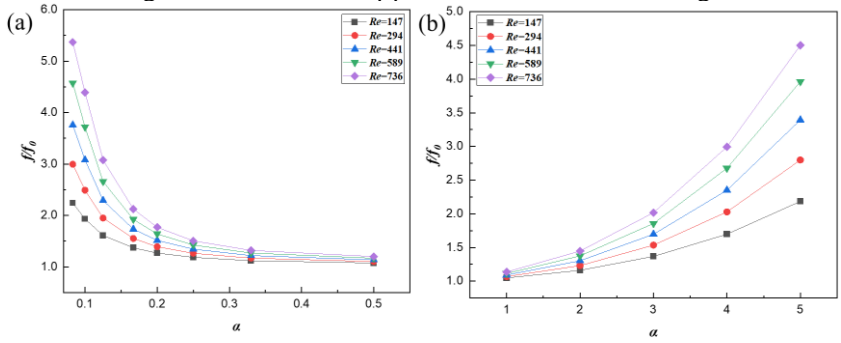

Figure 10. Variation of friction factor ratio f/f_0 of MC- PW with amplitude ratio α at (a) $\alpha < 1$, (b) $\alpha \geq 1$

As shown in Figure 11, the heat transfer performance is better than MC-RC for different wavy microchannels. In range of α from 0.25 to 0.5, Nu/Nu_0 increases with decreasing α. When α is less than 0.25, Nu/Nu_0 increases rapidly as α decreases. In the range of α from 1 to 5, Nu/Nu_0 increases with increasing α.

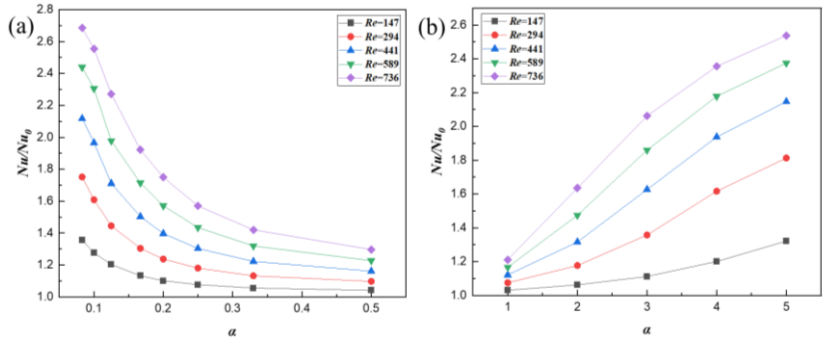

Figure 11. Variation of Nusselt number ratio Nu/Nu_0 of MC- PW with amplitude ratio α at (a) $\alpha < 1$, (b) $\alpha \geq 1$

As shown in Figure 12, when $0.125 < \alpha < 0.5$, the *PEC* increases approximately linearly with the decrease of α, $\alpha = 0.1$, and the *PEC* takes the maximum value of 1.56. When Re = 736, $\alpha < 0.125$, the *PEC* of MC-PW gradually decreases as α decreases, In the range of $1 < \alpha < 3$, the *PEC* increases with the increase of α. When $\alpha > 3$, the friction factor increases rapidly, which slows down the increase of the *PEC*, $\alpha = 4$, and the *PEC* takes the maximum value of 1.64. When Re = 736, $\alpha < 4$, the *PEC* of MC-PW increases with the increase of α. When Re = 736, $\alpha > 4$, the *PEC* of MC-PW decreases with increase of α. Comprehensive performance factor of the wavy microchannel is affected by the structure of the wavy, and the pressure drop of the wavy microchannel increases greatly, which makes comprehensive performance factor of the microchannel decrease.

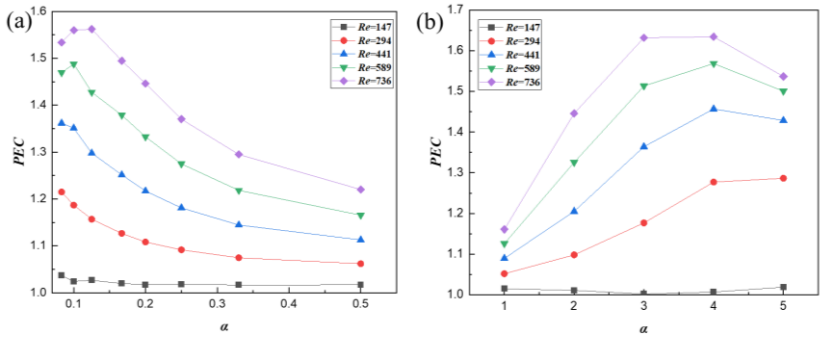

Figure 12. Variation of comprehensive performance factor *PEC* of MC- PW with amplitude ratio α at (a) $\alpha < 1$, (b) $\alpha \geq 1$

5. Conclusions

Wavy microchannels achieve better heat transfer performance at relatively low flow friction. At α = 0.25, Re = 736, the Nusselt number is improved by 9.48%, while the friction factor is increased by 56.9% for the symmetric structure compared to the parallel structure. At Re = 736, the Nusselt number is improved by 38.9%, while the friction factor is increased by 87.4% for the symmetric structure compared to the parallel structure.

(1) In MC-SW, the fluid exhibits recirculation at the trough positions, generating vortices and forming recirculation zones. These vortices enhance the fluid mixing and thus improve heat transfer. When amplitude ratio α is 3, MC-SW has the best comprehensive performance with *PEC* = 1.61 at Re = 736.

(2) The curved walls affect the flow characteristics within the MC-PW. The periodic arrangement of the wavy structure causes boundary layer interruption at each wave crest, followed by redevelopment. This cyclical disruption and redevelopment of the boundary layer enhance heat transfer. When the amplitude ratio α is 4, MC-PW has the best comprehensive performance with *PEC* = 1.64 at Re = 736.

Acknowledgment

This work was supported by the National Key Research and Development Program Project:"China-Sudan Joint Laboratory on a Novel Photovoltaic Ecological Agriculture(No. 2023YFE0126400) ".

Nomenclature

A_{con} - convection heat transfer area, [m^2]
A_q - surface areas at the bottoms of a single channels, [m^2]
$C_{p,f}$ - specific heat of the fluid, [$Jkg^{-1}K^{-1}$]
D_h- hydraulic diameter, [mm]
f- friction factor
H - height of computational domain, [mm]
H_c - height of channel, [mm]
h_m- average heat transfer coefficient, [$Wm^{-2}K^{-1}$]
K - thermal conductivity
k_f- thermal conductivity of the fluid, [$Wm^{-1}K^{-1}$]
L - length of heat sink, [mm]
Nu - Nusselt number
PEC - comprehensive performance factor
P_o - Poiseuille number
q_w - heat flux at the bottom of heat sink, [Wm^{-2}]
Re - Reynolds number
T - temperature, [K]

u,v,w - velocity components, [m^{-1}]
u_m - Average velocity of fluid, [m^{-1}]
W - width of computational domain, [mm]
W_C - width of channel, [mm]
Δp - pressure drop, [Pa]

Greek symbols

α - amplitude ratio
α_c - aspect ratio
μ - dynamic viscosity, [m^2s^{-1}]
p - density of fluid, [kgm^{-3}]
λ- wave length, [mm]

Subscripts

f - fluid
s - solid
w - wall
0 - straight rectangular channel

References

[1] Tuckerman, D. B., Pease, R. F.W., High-Performance Heat Sinking for VLSI, *IEEE Electron Device Letters*, 2(1981), 5, pp. 126-129.

[2] Wang, X. D., *et al*., Optimal Geometric Structure for Nanofluid-Cooled Microchannel Heat Sink Under Various Constraint Conditions, *Energy Conversion and Management*, 65(2013), pp. 528-538.

[3] Leng, C., *et al*., An Improved Design of Double-Layered Microchannel Heat Sink with Truncated Top Channels, *Applied Thermal Engineering*, 79(2015), pp. 54-62.

[4] Shang, X. S., *et al*., Mathematical Modeling and Multi-Objective Optimization on The Rectangular Micro-Channel Heat Sink, *International Journal of Thermal Sciences*, 184(2023), pp. 107926.

[5] Kumar, K., Kumar, P., Effect of Groove Depth on Hydrothermal Characteristics of The Rectangular Microchannel Heat Sink, *International Journal of Thermal Sciences*, 161(2021), pp. 106730.

[6] Zhu, Q. F., *et al*., Local Hydrothermal Characteristics and Temperature Uniformity Improvement of Microchannel Heat Sink with Non-Uniformly Distributed Grooves, *Case Studies in Thermal Engineering*, 47(2023), pp. 103113.

[7] Soo, Y., H., et al., Heat transfer enhancement of staggered water-droplet grooved microchannel heat sink using Al_2O_3 nanofluid. *Thermal Science*, 28(2024), 3 Part B, pp. 2477-2490.

[8] Bhandari P., et al. Design modifications in micro pin fin configuration of microchannel heat sink for single phase liquid flow: A review. *Journal of Energy Storage*, 66(2023), 107548.

[9] Bhandari P., Prajapati Y K. Influences of tip clearance on flow and heat transfer characterstics of open type micro pin fin heat sink. *International Journal of Thermal Sciences*, 179(2022), 107714.

[10] Bhandari P, Prajapati Y K. Thermal performance of open microchannel heat sink with variable pin fin height. *International journal of thermal sciences*, 159(2021), 106609.

[11] Wang, R. J., *et al*., Parameterization Investigation on The Microchannel Heat Sink with Slant Rectangular Ribs by Numerical Simulation, *Applied Thermal Engineering*, 133(2018), pp. 428-438.

[12] Khoshvaght-Aliabadi, M. *et al*., Performance Enhancement of Straight and Wavy Miniature Heat Sinks Using Pin-Fin Interruptions and Nanofluids, *Chemical Engineering and Processing: Process Intensification*, 122(2017), pp. 90-108.

[13] Venkiteswaran, V. K., et al., Comparative study of heat and fluid flow characteristics of parallel and offset strip fin micro-channels using CFD simulations. *Thermal Science*,22 (2018), 5, pp. 1973-1985.

[14] Li, H., *et al*., Optimal Design of Microchannel Heat Sink with Staggered Fan-Shaped Cavities and Ribs, *Journal of Thermophysics and Heat Transfer*, 38(2024), 2, pp. 145-158.

[15] Wang, C.L., et al. Enhanced heat transfer study of microchannel heat sink with periodically arranged triangular cavities and arc-shaped ribs. *Heat Transfer*, 53(2024), 5, pp. 2438-2459.
[16] Datta, A., *et al*., A Conjugate Heat Transfer Analysis of Performance for Rectangular Microchannel with Trapezoidal Cavities and Ribs, *International Journal of Thermal Sciences*, 138(2019), pp. 425-446.
[17] Zhu, Q. F., *et al*., Numerical Simulation Study of Thermal and Hydraulic Characteristics of Laminar Flow in Microchannel Heat Sink with Water Droplet Cavities and Different Rib Columns, *International Journal of Thermal Sciences*, 172(2022), pp. 107319.
[18] Jiang, M. X., Pan, Z. L., Optimization of micro-channel heat sink based on genetic algorithm and back propagation neural network. *Thermal Science*, 27(2023), 1 Part A, pp. 179-193.
[19] Sui, Y., *et al*., Fluid Flow and Heat Transfer in Wavy Microchannels, *International Journal of Heat and Mass Transfer*, 53(2010), pp. 2760-2772.
[20] Sui, Y., *et al*., Direct Numerical Simulation of Fluid Flow and Heat Transfer in Periodic Wavy Channels with Rectangular Cross-Sections, *International Journal of Heat and Mass Transfer*, 55(2012), 1-3, pp. 73-88.
[21] Sui, Y., et al., An Experimental Study of Flow Friction and Heat Transfer in Wavy Microchannels with Rectangular Cross Section, I*nternational journal of thermal sciences*, 50(2011), 12, pp. 2473-2482.
[22] Xie, G. N., *et al*., Constructal Theory Based Geometric Optimization of Wavy Channels in The Low Reynolds Number Regime, *Journal of Electronic Packaging*, 136(2014), 3, pp. 031013.
[23] Zhou, J. D., *et al*., Design of Microchannel Heat Sink with Wavy Channel and Its Time-Efficient Optimization with Combined RSM and FVM Methods, *International Journal of Heat and Mass Transfer*, 103(2016), pp. 715-724.
[24] Ali, A. Y. M., *et al*., Thermal Analysis of High Concentrator Photovoltaic Module Using Convergent-Divergent Microchannel Heat Sink Design, *Applied Thermal Engineering*, 183(2021), pp. 116201.
[25] Wang, X. W., *et al*., Study on The Flow and Heat Transfer Characteristics of Sinusoidal Half-Corrugated Microchannels, *Journal of Thermophysics and Heat Transfer*, 34(2020), 2, pp. 314-321.
[26] Fang, Y. Q., et al., Numerical study on heat and flow transfer characteristics in rectangular minichannel with S-shaped turbulator inserted. *Thermal science*, 27(2023), 4 Part A, pp. 2865-2877.
[27] Steinke, M. E., Kandlikar, S. G., Single-Phase Liquid Friction Factors in Microchannels, *International journal of thermal sciences*, 45(2006), 11, pp. 1073-1083.
[28] Phillips, R. J., Microchannel Heat Sinks, *The Lincoln Laboratory Journal*, 1(1988), 1, pp. 31-48
[29] Liu., W., *et al*., Physical Quantity Synergy in Laminar Flow Field and Its Application in Heat Transfer Enhancement, *International Journal of Heat and Mass Transfer*, 52(2009), 19-20, pp. 4669-4672.
[30] Bhandari P., et al. A review on design alteration in microchannel heat sink for augmented thermo-hydraulic performance. *Ain Shams Engineering Journal*, 15(2024), (2): 102417

Received: 6.12.2024.
Revised: 11.6.2025.
Accepted: 28.6.2025.